

Gold Nanobipyramid-Supported Silver Nanostructures with Narrow Plasmon Linewidths and Improved Chemical Stability

Xingzhong Zhu, Xiaolu Zhuo, Qian Li, Zhi Yang,* and Jianfang Wang*

Silver nanostructures with narrow plasmon linewidths and good chemical stability are strongly desired for plasmonic applications. Herein, a facile method is discussed for the preparation of Ag nanostructures with narrow plasmon linewidths and improved chemical stability through Ag overgrowth on monodispersed Au nanobipyramids. Structural evolution from bipyramid through rice to rod is observed, indicating that Ag atoms are preferentially deposited on the side surfaces of Au nanobipyramids. The resultant (Au nanobipyramid)@Ag nanostructures possess high size and shape uniformities, and much narrower plasmon linewidths than other Ag nanostructures. The spectral evolution of the supported Ag nanostructures is ascertained by both ensemble and single-particle characterizations, together with electrodynamic simulations. Systematic measurements of the refractive index sensing characteristics indicate that Ag nanostructures in this study possess high index sensitivities and figure of merit (sensitivity divided by linewidth) values. Moreover, Ag nanostructures in this study exhibit greatly improved chemical stability. The superior sensing capability of Ag nanostructures in this study is further demonstrated by the detection of sulfide ions at a relatively low detection limit. Taken together, results of this study show that the Au-nanobipyramid-supported Ag nanostructures will be an outstanding candidate for the design of ultrasensitive plasmonic sensing devices as well as for the development of other plasmon-enabled technological applications.

attention in the past two decades owing to its fascinating ability of confining light at the nanoscale. The localized plasmon modes of Au and Ag nanostructures are highly tunable over a wide spectral range from the visible to near-infrared region, which has enabled widespread potential applications of noble metal nanostructures in nanooptics,^[1] chemical/biological sensing,^[2,3] photocatalysis,^[4] photothermal therapeutics,^[5] solar energy harvesting,^[6] and surface-enhanced spectroscopies.^[7]

Owing to the unique dielectric function of Ag, Ag nanostructures possess the highest plasmonic activity among different metals, which is advantageous for various plasmonic applications. Owing to the joint effect of the real part of the dielectric function and its spectral dispersion, Ag nanostructures exhibit higher refractive index sensitivities than Au nanostructures in the visible and near-infrared regions.^[8–11] The plasmon-enabled field enhancements of Ag nanostructures are usually larger than those of Au ones with similar shapes and sizes, which makes Ag nanostructures superior to Au ones in surface-enhanced

Raman and fluorescence applications.^[12,13] Ag nanostructures also exhibit larger solar energy conversion efficiencies than Au nanostructures.^[14] Therefore, Ag nanostructures are very attractive in various plasmon-based technological applications. Many excellent results have been obtained by use of Ag nanostructures. For example, a refractive index sensitivity (RIS) of 1096 nm RIU^{−1} (refractive index unit) at the in-plane dipolar plasmon wavelength of 1093 nm has been determined for triangular Ag nanoplates, suggesting that they are good candidates for developing ultrasensitive plasmonic sensing devices.^[15] Ag overgrowth on Au nanorods has been shown to be kinetically programmable, and has been employed to fabricate time-temperature indicators for monitoring the quality of perishable products.^[16] (Au core)@(Ag shell) nanostructures have been explored as highly sensitive intracellular sulfide probes.^[17] The detection limit at the single-particle level reaches as low as 0.01×10^{-9} M.

Despite their outstanding plasmonic performances as mentioned above, Ag nanostructures suffer from two major drawbacks, making them disadvantageous for many practical

1. Introduction

Localized surface plasmon resonance, that is, the collective oscillation of electrons in noble metal nanostructures in resonance with an incident electromagnetic field, has received much

X. Z. Zhu, Prof. Z. Yang
Key Laboratory for Thin Film and Microfabrication
of Ministry of Education
Department of Micro/Nano Electronics
School of Electronic Information
and Electrical Engineering
Shanghai Jiao Tong University
Shanghai 200240, China
E-mail: zhiyang@sjtu.edu.cn

X. L. Zhuo, Dr. Q. Li, Prof. J. F. Wang
Department of Physics
The Chinese University of Hong Kong
Shatin, Hong Kong SAR, China
E-mail: jfwang@phy.cuhk.edu.hk



DOI: 10.1002/adfm.201503670

applications. First, although the syntheses of a number of Ag nanostructures have been demonstrated, Ag nanostructures with strong, narrow plasmon bands in the visible and near-infrared regions have still remained limited. Inhomogeneous distributions of Ag nanostructures in shape and size give rise to relatively large ensemble plasmon linewidths, which are usually characterized with the full widths at half maximum (FWHMs). Of Ag nanostructures that have been reported so far with synthetically tunable plasmon wavelengths, Ag nanoplates possess the narrowest ensemble plasmon linewidths (Table S1, Supporting Information), with values of 0.22–0.36 eV in aqueous solutions.^[18] Such plasmon linewidths are still broad in comparison with those of single Ag nanostructures. Second, the poor chemical and structural stability of Ag nanostructures is also a drawback for practical applications. Unprotected Ag nanostructures are unstable thermodynamically. Their sharp edges are often rounded automatically when stored in aqueous solutions.^[19,20] These two obstacles severely hinder the realization of the full potential of Ag nanostructures in many plasmonic applications. Therefore, methods are still strongly desired for the preparation of Ag nanostructures with narrow plasmon linewidths and improved chemical stability.

In this work, we produce Ag nanostructures with narrow plasmon linewidths and improved chemical stability through Ag overgrowth on Au nanobipyramids (NBPs). The plasmon wavelengths of the produced Au NBP@Ag nanostructures vary with the increase of the Ag precursor amount. Ag atoms are found to grow preferentially on the side surfaces of the Au NBPs. The length of the nanostructures is nearly identical to that of the Au NBPs and the diameter becomes slightly larger. The shape of the Au NBP@Ag nanostructures therefore evolves from bipyramid through rice to rod. During the overgrowth process, the plasmon linewidths of the Au NBP@Ag nanostructures show gradual increases as more Ag precursor is supplied. The dependences of the RIS and figure of merit (FOM, sensitivity divided by linewidth) values of the Au NBP@Ag nanostructures are systematically examined as functions of the Ag precursor amount. The RIS and FOM values of the nanostructures can be separately maximized to be larger than those of the Au NBPs by optimizing the Ag precursor amount. Moreover, the stability of the nanostructures in aqueous solutions is clearly improved in comparison with Ag nanoplates with a close ensemble plasmon wavelength. The superior sensing characteristics of the Au NBP@Ag nanostructures are finally demonstrated by the detection of sulfide ions, with a detection limit as low as 0.1×10^{-6} M.

2. Results and Discussion

2.1. Gold NBP-Supported Growth of Silver Nanostructures

A combination of seed-mediated growth and Ag overgrowth was utilized to prepare the Au NBP-supported Ag nanostructures, with cetyltrimethylammonium bromide (CTAB) and cetyltrimethylammonium chloride (CTAC) as the stabilizing agents, respectively. The starting Au NBP sample was produced and purified using seed-mediated growth and depletion force-induced separation, respectively, as described in our previous

works.^[21,22] Au NBPs were chosen as the support owing to their excellent size and shape uniformities. The number percentages of purified Au NBPs approach 100%. Each Au NBP is made up of two pentapyramids, which are base-to-base connected.^[22–24] In each Au NBP, there are five twinning planes, which are all aligned parallel to the length axis and equally angularly separated around the length axis. Owing to their particular crystalline structure, the relative standard deviations of Au NBPs in length and middle diameter are in the ranges of 3%–9% and 3%–11%, respectively. For example, because of the high shape and size uniformities, the FWHM value of the longitudinal plasmon peak at 680 nm for an ensemble Au NBP sample is 60 nm, only 12 nm larger than that of the single Au NBPs from the same batch of the sample.^[22] In comparison, for a typically prepared Au nanorod sample with the same longitudinal plasmon wavelength, the ensemble FWHM value of the longitudinal plasmon peak is 105 nm, about twice the corresponding single-particle value. In fact, among all reported Au nanostructures, the plasmon peak widths of Au NBPs are the narrowest at the ensemble level (Table S2, Supporting Information). The longitudinal plasmon wavelengths of Au NBPs can be synthetically tuned from 700 to 1200 nm by varying the volume ratio between the seed and growth solutions. Considering that ≈ 800 nm is the most commonly used wavelength in the first near-infrared biological transparency window, metal nanostructures with plasmon wavelengths around 800 nm will be useful for many biotechnological applications.^[25,26] We therefore chose Au NBPs with their longitudinal plasmon wavelength around 800 nm as a candidate to prepare the Au NBP@Ag nanostructures in our work.

The overgrowth of Ag on the Au NBPs was realized through the reduction of AgNO_3 by ascorbic acid in the presence of CTAC, following our previous procedure for the synthesis of (Au nanorod core)@(Ag shell) nanocuboids from single-crystalline Au nanorods.^[27] Figure 1a shows schematically the shape evolution of the nanostructures during Ag overgrowth. Ag atoms are first deposited on the side surfaces, enlarging the thinner segments. As more Ag atoms are deposited, the nanostructures become cylindrical, with the Au NBP encapsulated at the center. The extinction spectra of the nanostructures obtained by adding different amounts of AgNO_3 are shown in Figure 1b. For these extinction spectra, the dilution caused by the addition of the AgNO_3 and ascorbic acid solutions has been corrected. The particle concentrations in the solutions are therefore the same for all of the samples. The longitudinal and transverse dipolar plasmon modes of the starting Au NBP sample are located at 805 and 512 nm, respectively. With Ag overgrowth, the longitudinal and transverse plasmon modes of the Au NBP@Ag nanostructures first blueshift, owing to the increasing effect of the optical properties of Ag over those of Au, which has been elucidated in our previous work on Ag overgrowth on Au nanorods.^[27] The plasmon shifts induced by metal overgrowth depend on the specific type of the metal. For example, Pd overgrowth on Au nanocrystals causes a red shift on the plasmon resonance.^[28] In our study, the blue shift continues until the added volume of the AgNO_3 solution reaches 90 μL . When the AgNO_3 volume is above 90 μL , the longitudinal plasmon peak starts to redshift. Such a variation arises mainly from the evolution of the shape of the nanostructures instead of

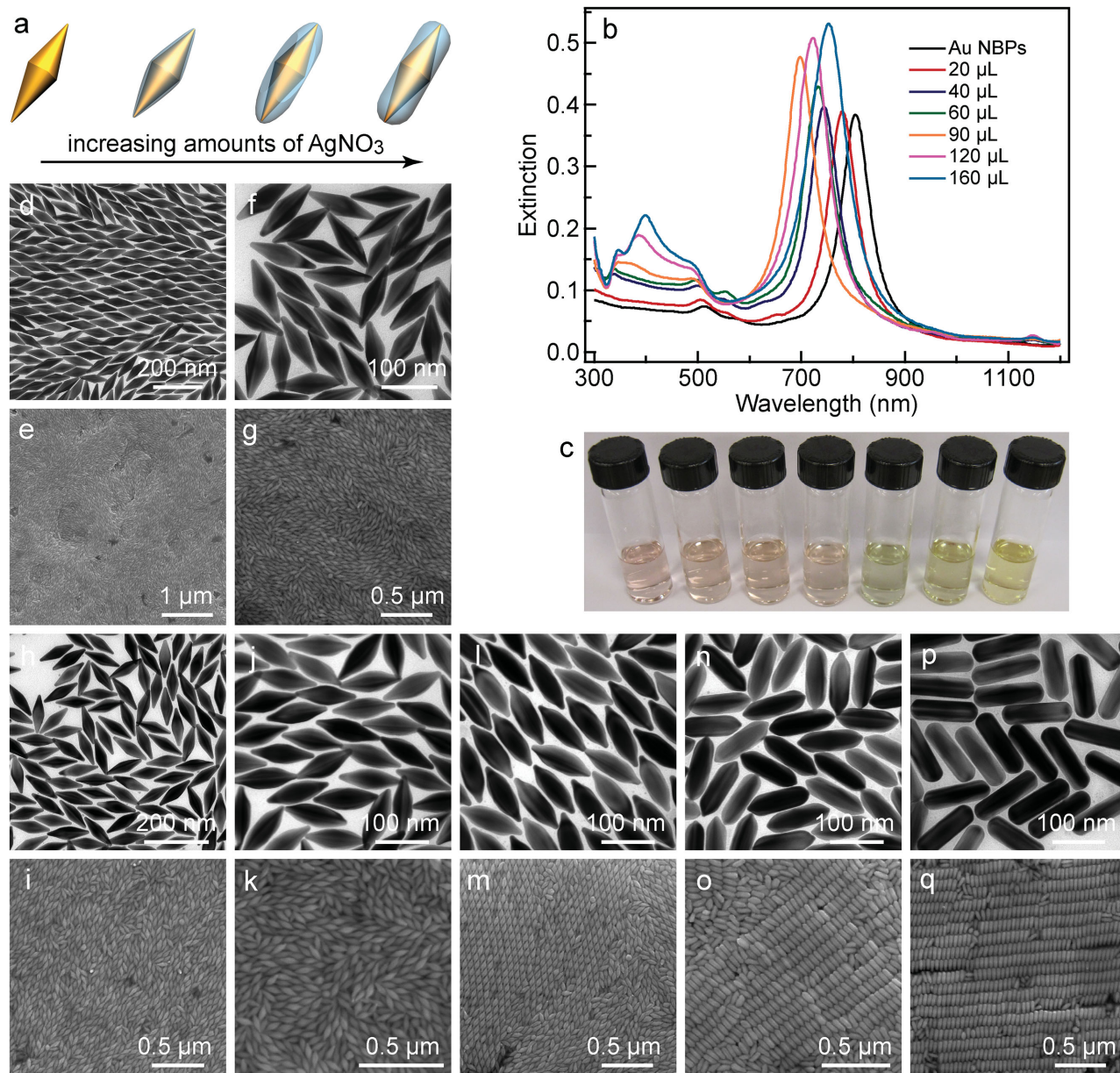


Figure 1. Gold NBP-supported silver nanostructures. a) Schematic illustrating Ag overgrowth on the Au NBPs. b) Extinction spectra of the Au NBP and Au NBP@Ag nanostructure samples grown with varying amounts of AgNO₃. c) Digital photograph of the colloidal solutions of the Au NBP and Au NBP@Ag nanostructure samples. The samples from left to right correspond to those produced with the increasing AgNO₃ amounts. d–q) TEM and SEM images of the Au NBP and Au NBP@Ag nanostructure samples produced with 20, 40, 60, 90, 120 and 160 µL of AgNO₃ (0.01 M), respectively. A total of seven samples are shown. For each sample, on the top is the TEM image and at the bottom is the SEM image.

the optical properties of Ag. For all of the AgNO₃ volumes used in our overgrowth experiments, the transverse plasmon peak stays around 500 nm and blueshifts slightly. When the AgNO₃ volume is above 90 µL, two new peaks emerge around 400 and 350 nm. They can be attributed to the transverse multipolar plasmon mode of the Au NBP@Ag nanostructures and the plasmon resonance of bulk Ag, respectively.^[22,27] The extinction intensities of all of the four plasmon bands increase with the AgNO₃ amount. In addition, the 60 µL Au NBP@Ag nanostructure sample also exhibits a discernible peak around 550 nm. This peak can be ascribed to a higher-order longitudinal

plasmon mode. The occurrence of the higher-order longitudinal plasmon modes has been found to be very sensitive to the size and exact shape of the Au NBPs.^[22] The spectral evolution of the plasmon modes gives rise to vivid color changes for the colloidal nanostructure solutions (Figure 1c).

The Au NBP@Ag nanostructures grown with different amounts of AgNO₃ were imaged under both transmission electron microscopy (TEM) and scanning electron microscopy (SEM) (Figure 1d–q). Their sizes were measured on the acquired TEM images. The imaging results show that the starting Au NBPs and the produced Au NBP@Ag nanostructures possess

uniform morphologies and narrow size distributions. The purified Au NBP sample used in this study has an average length of 122 ± 4 nm and diameter of 39 ± 2 nm, where the diameters were measured at the middle. The average lengths/diameters of the Au NBP@Ag nanostructures grown with 20, 40, 60, 90, 120 and 160 μL of the AgNO_3 solution are 122 ± 3 nm/ 39 ± 2 nm, 121 ± 4 nm/ 39 ± 2 nm, 122 ± 4 nm/ 40 ± 2 nm, 123 ± 4 nm/ 41 ± 1 nm, 123 ± 4 nm/ 41 ± 2 nm and 122 ± 3 nm/ 41 ± 2 nm, respectively. As the AgNO_3 amount is increased, the Au NBP@Ag nanostructures gradually change from the bipyramid shape through a rice shape to a final cylindrical rod shape, which verifies the schematic models shown in Figure 1a. Moreover, all of the produced nanostructure samples are highly pure, with their number percentages approaching 100%. The high purities are enabled by two factors. One is that our starting Au NBP sample is highly pure. The other is that no self-nucleation occurs in the overgrowth process. Ag^+ ions are only reduced and deposited on the surfaces of the Au NBPs. The high purity and high dimensional uniformity allows the nanostructures to pack into highly ordered structures, as shown in Figure 1m,o,q. The formation of such highly ordered superstructures has been found to be dependent on the surfactant type and concentration, the shape and dimensional uniformities of nanoparticles, and the solvent evaporation conditions.^[29–31]

To better ascertain the overgrowth process, we performed high-angle annular dark-field scanning transmission electron microscopy (HAADF-STEM) imaging and elemental mapping on the Au NBP@Ag nanostructures (Figure 2a–d and Figure S1, Supporting Information). With these imaging techniques, the structure and composition of the nanostructures can be obtained simultaneously. The elemental mapping shows clearly that each nanostructure contains a gold NBP at the center, with Ag atoms located on the side surfaces of the Au NBP. This preferential deposition of Ag atoms is because the side surfaces of the Au NBPs are high-index-faceted.^[24,32,33] The deposition of Ag atoms on these facets can lower their surface energies. To quantify the amount of Ag deposited on the Au NBPs, inductively coupled plasma atomic emission spectrometry (ICP-AES) measurements were carried out on the Au NBPs and Au NBP@Ag nanostructures. The particle concentrations in the different sample solutions were maintained to be the same for the ICP-AES measurements. The Au and Ag mass concentrations in the samples were determined according to the calibration lines determined in advance from the standard Au and Ag solutions (Figure S2, Supporting Information). The obtained Au and Ag molar concentrations for the seven samples are listed in Table S3 in the Supporting Information. The Ag molar concentrations in the samples were determined to be $(3.7\text{--}34.1) \times 10^{-6}$ M. The presence of Ag in the starting Au NBP sample is because AgNO_3 is employed in the seed-mediated growth to increase the number yields of elongated Au nanocrystals.^[21,34,35] As shown in Figure 2e, the Ag-to-Au molar ratios of the nanostructures are linearly dependent on the AgNO_3 volume. From the linear dependence, we can estimate that $\approx 48\%$ of Ag added in the growth solution is reduced and grown onto the Au NBPs. Such a specific relationship makes it convenient to produce desired Au NBP@Ag nanostructures by simply adjusting the added AgNO_3 amount.

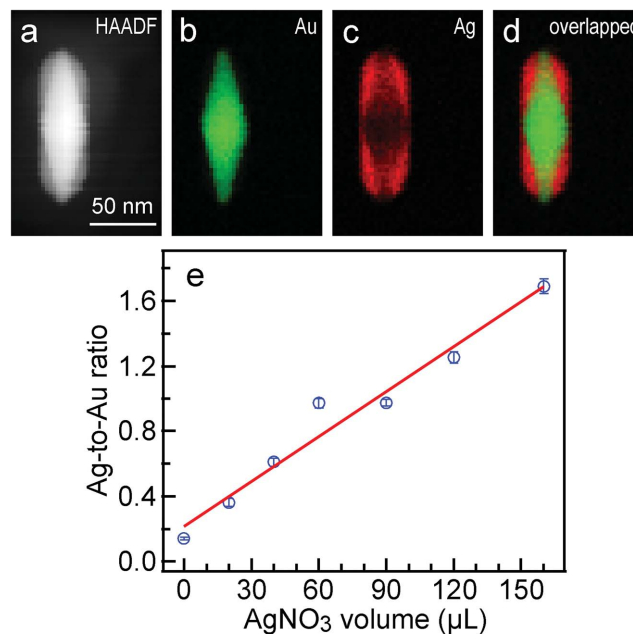


Figure 2. HAADF-STEM characterization and the Ag-to-Au molar ratio of the Au NBP@Ag nanostructures. a) HAADF-STEM image of a single 120 μL Au NBP@Ag nanostructure. b,c) Elemental mapping images of Au and Ag on the nanostructure shown in panel (a), respectively. d) Overlapped image. The scale bar in panel (a) also applies for panels (b–d). e) Dependence of the measured Ag-to-Au molar ratios of the Au NBP@Ag nanostructure samples on the added volume of the AgNO_3 solution. The coefficient of determination for the linear fitting is $R^2 = 0.9655$. The error bar height for each point represents one standard deviation.

2.2. Variations of the Plasmon Peak Position and Linewidth in Wavelength and Energy

We have shown in our previous work that ensemble Au NBP samples possess much narrower plasmon peak widths than ensemble Au nanorod samples, mainly owing to their high shape and size uniformities.^[22] For many potential plasmonic applications, the Au NBP@Ag nanostructures are highly desired to maintain the uniformities and therefore narrow plasmon peak widths in the Ag overgrowth process. In this regard, we carefully investigated the dependences of the sizes, plasmon wavelengths and linewidths of the Au NBP@Ag nanostructures on the added AgNO_3 volume. The use of the same starting Au NBP sample for all Ag overgrowths allows for quantitative comparison among the seven nanostructure samples. In addition, only the longitudinal dipolar plasmon mode was considered, because it is much stronger than the other plasmon modes and its wavelength is mainly determined by the length-to-diameter aspect ratio. The average lengths and diameters measured from the TEM images are plotted in Figure 3a as functions of the added AgNO_3 volume. The obtained Au NBP@Ag nanostructures possess narrow size distributions with relative standard deviations of 3%–5%. During Ag overgrowth, the lengths remain nearly unchanged while the diameters undergo a slight increase. Such size variations suggest that Ag atoms are preferentially deposited on the side surfaces of the Au NBPs to transform the bipyramid shape into the rod shape. After

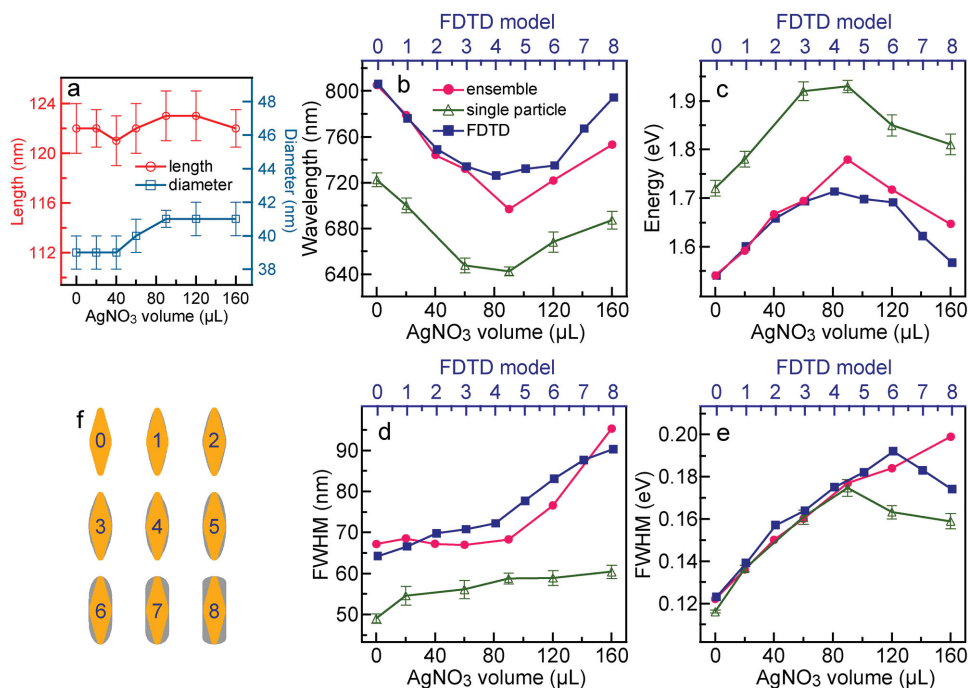


Figure 3. Sizes, longitudinal dipolar plasmon wavelengths, and linewidths of the Au NBP@Ag nanostructure samples. a) Length (left, red) and diameter (right, blue) changes as functions of the added AgNO₃ volume. b) Variations of the longitudinal dipolar plasmon wavelengths. The solid red circles, hollow green triangles, and solid blue squares represent the data points for the ensemble samples, single-particle values, and FDTD-simulated results, respectively. c) Variations of the longitudinal dipolar plasmon energies. d) Variations of the longitudinal dipolar plasmon linewidths in wavelength. e) Variations of the longitudinal dipolar plasmon linewidths in energy. f) Schematic illustrating the models utilized in the FDTD simulations. The labeling numbers for the models were used as the x-axis values in plotting the simulated data points in (b–e). The symbols in (c–e) have the same meanings as those in (b). The error bar height for each data point represents one standard deviation.

the nanostructures assume the rod shape, further addition of AgNO₃ will cause the nanorods to grow longer, producing Ag nanorods with variable lengths. We have described the growth of Ag nanorods by this method and discussed their multipolar plasmon properties in a separate report.^[36] Remarkably, the high dimensional uniformity of the Ag nanorods allows for the observation and study of sharp multipolar plasmon modes at the ensemble level in colloidal solutions.

The plasmon linewidths of ensemble metal nanoparticles contain contributions from both inhomogeneous and homogeneous line broadening. Inhomogeneous line broadening is mainly caused by shape and size distributions. High shape and size uniformities are required for minimizing or eliminating the inhomogeneous line broadening of ensemble metal nanoparticles. For homogeneous line broadening, a narrower plasmon peak width implies a smaller plasmon damping and a larger local electric field enhancement.^[37] Homogeneous plasmon linewidths play a paramount role in many plasmon-based applications, such as monitoring electron transfer between metal nanoparticles and other materials,^[38] studying chemical bonding on metal nanoparticles,^[39] and developing ultrasensitive chemical and biological sensors.^[2] In most studies, the data points for plasmon wavelengths and linewidths are analyzed and reported in wavelength with the unit of nanometer. In our study, apart from the wavelength values, we also provided the corresponding energy values in order to facilitate the understanding and unraveling of the underlying variation trends. The longitudinal dipolar plasmon wavelengths and linewidths

of the ensemble nanostructures were obtained by Lorentzian curve fitting of the extinction spectra in Figure 1b. For the corresponding energy values, the extinction spectra were replotted by changing the wavelength values to the energy ones for the x-axis before the curve fitting. With the increase of the added AgNO₃ amount, the ensemble plasmon wavelength first blueshifts and then redshifts, with the turning point located at 90 μL, which is a minimum on the wavelength plot (Figure 3b) but a maximum on the energy plot (Figure 3c). On the wavelength plot, the ensemble FWHM values of the Au NBP@Ag nanostructures are almost constant at ≈67 nm before the turning point, and increase after the turning point (Figure 3d). On the energy plot, however, the ensemble FWHM values increase gradually with increasing AgNO₃ amounts for all overgrowths (Figure 3e).

In order to eliminate the possible inhomogeneous line broadening effect associated with the ensemble measurements, we further recorded the single-particle scattering spectra of the Au NBP@Ag nanostructures by dark-field scattering spectroscopy.^[40] The nanostructures were deposited on glass slides at appropriate surface number densities, which were verified by dark-field scattering imaging (Figure 4a). Figure 4b shows five typical spectra of the 120 μL Au NBP@Ag nanostructure sample. The spectra of the other samples are provided in Figure S3 in the Supporting Information. The scattering spectra of more than 60 individual nanoparticles were acquired for each sample. The peak positions and widths in both wavelength and energy for the longitudinal plasmon mode were determined similarly

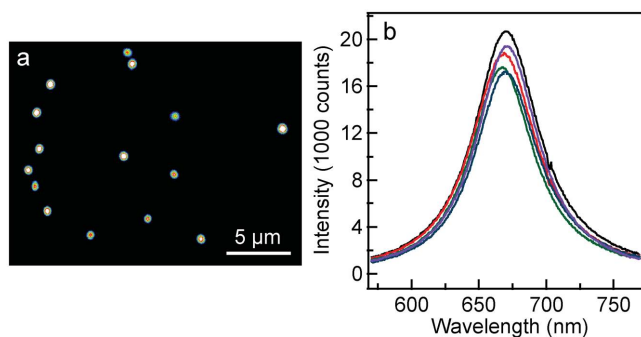


Figure 4. Dark-field scattering results of the 120 μL Au NBP@Ag nanostructure sample. a) Representative scattering image. b) Five representative single-particle scattering spectra.

by Lorentzian curve fitting. The obtained values were then averaged and plotted as functions of the added AgNO_3 volume in Figure 3b–e. The small standard deviations in the longitudinal plasmon peak positions reflect that the Au NBP@Ag nanostructures have narrow shape and size distributions. The overall variation trends of the plasmon positions obtained from the single-particle measurements are very similar to those obtained from the ensemble extinction measurements. However, for all samples, the average plasmon wavelengths determined from the single-particle measurements are smaller than the corresponding ensemble values (Figure 3b,c). The shorter plasmon wavelengths and therefore higher plasmon energies are caused by the change of the surrounding medium from water in the ensemble measurements to a non-uniform environment of air and glass in the single-particle measurements. In the case of the peak widths in wavelength, the FWHM values increase gradually (Figure 3d). The single-particle FWHM values are all smaller than the corresponding ensemble ones. In contrast, on the energy plot, the single-particle FWHM values first increase up to the turning point at 90 μL and then start to decrease (Figure 3e). Moreover, the single-particle FWHM values are almost identical to the corresponding ensemble values up to the turning point, but become smaller than the corresponding ensemble ones after the turning point. There are two implications from these results. First, the plasmon linewidth in wavelength is inherently dependent on the plasmon wavelength. As the plasmon wavelength gets shorter, the plasmon linewidth in wavelength generally becomes smaller. This dependence complicates the variation trend of the plasmon linewidths in wavelength. Second, before the turning point, the contribution of inhomogeneous line broadening to the plasmon linewidths is very small, suggesting that the related Au NBP@Ag nanostructure samples are highly uniform in shape and size. Only after the turning point, does the contribution of inhomogeneous line broadening become apparent and get larger. The inhomogeneous line broadening arises probably from the shape distributions because a relatively large amount of Ag atoms are deposited on the Au NBPs for these nanostructure samples.

Finite-difference time-domain (FDTD) simulations were also performed to assist in understanding the evolutions of the structural and plasmonic properties of the Au NBP@Ag nanostructures with increasing AgNO_3 amounts. The geometrical models utilized in the FDTD simulations were set according

to the shapes observed on the TEM images, but the exact correspondence of a simulation model to a nanostructure sample prepared with a specific amount of AgNO_3 was not pursued, due to the limited spatial resolution under the HAADF-STEM imaging. The length and diameter of the Au NBP were set at 122 and 39 nm, and those of the Au NBP@Ag nanostructures were 122 and 42 nm, respectively, with Ag atoms increasingly added on the side surfaces of the Au NBP, as shown in Figure 3f. The excitation light direction was perpendicular to the length axis, with the electric field polarized along the length axis. Therefore, only the longitudinal plasmon mode was excited. The refractive index of the surrounding medium was set at 1.33, the refractive index of water. We considered only the longitudinal dipolar plasmon mode and extracted the plasmon positions and linewidths in both wavelength and energy by Lorentzian curve fitting of the simulated extinction spectra. In general, the simulated variation trends are in agreement with the experimental ensemble observations for the plasmon wavelengths, plasmon energies and plasmon linewidths in wavelength (Figure 3b–d). The blue shifts on the longitudinal plasmon peak for the Au NBP@Ag nanostructures supported on glass slides in comparison with the corresponding ones immersed in water were verified by the FDTD simulations (Supporting Information, Figure S4). For the plasmon linewidths in energy, before the turning point, the simulated FWHM values are almost identical to the experimental ensemble values as well as to the measured single-particle values (Figure 3e). The nearly equal FWHM values in energy imply again the importance of using energy in studying the plasmon linewidth and the related effects, such as inhomogeneous contribution and plasmon damping. After the turning point, the simulated FWHM values differ from both the measured ensemble and single-particle values. We believe the discrepancy between the simulated and measured single-particle FWHM values is probably due to the limitation in modeling the exact geometry of the Au NBP@Ag nanostructures when a relatively large amount of Ag atoms is deposited on the Au NBPs. On the other hand, we also performed FDTD simulations by replacing the Ag part in the structure models with Au. The simulation results indicate that the optical properties of Ag indeed contribute to the blue shifts of the longitudinal dipolar plasmon resonance (Supporting Information, Figure S5). However, the longitudinal plasmon wavelength variations caused by the shape changes are larger than those arising from the different metals.

2.3. Refractive Index Sensitivity

Because of inhomogeneous line broadening, ensemble metal nanostructures are usually inferior to the corresponding single nanostructures in various sensing applications, especially where ultrahigh sensitivities are pursued. For our Au NBP@Ag nanostructures, due to their excellent monodispersity, the inhomogeneous broadening of their longitudinal plasmon peak is relatively small. The ensemble Au NBP@Ag nanostructures are therefore expected to show comparable sensing performances to those of the single nanostructures, making them attractive for sensing applications in solutions. RIS and FOM are two most important parameters for characterizing the

refractive index sensing capability of plasmonic metal nanostructures. RIS is defined as the slope of the linear dependence of the plasmon red shift on the refractive index of the surrounding medium. FOM is expressed as the ratio of the RIS to the plasmon linewidth.^[41] A high FOM brought about by a narrow linewidth is strongly desired, because it enables the detection of minuscule spectral changes. Therefore, narrow plasmon linewidths are also crucial for plasmonic sensing. To determine the RIS and FOM values of the Au NBP@Ag nanostructures, the nanostructures were dispersed in water–glycerol mixture solvents with the volume percentages of glycerol varied among 0%, 10%, 20%, 30%, 40%, 50%, 60%, 70%, 80%, and 90%. Pure glycerol was not used because it is too viscous. The refractive indices of water and glycerol are 1.3334 and 1.4746, respectively. The refractive indices of the liquid mixtures were calculated according to the Lorentz–Lorenz equation.^[42,43]

Figure 5a shows as an example the extinction spectra of the 20 μL Au NBP@Ag nanostructure sample dispersed in the liquid mixtures of varying compositions. To reveal more clearly the plasmon shifts, the spectra were plotted only in a narrow wavelength range containing the longitudinal plasmon peak. The extinction spectra in a wide spectral range for all of the seven samples are provided in Figure S6 in the Supporting Information. For all samples, the longitudinal plasmon peak exhibits red shifts as the volume percentage of glycerol is increased. The peak shifts display approximately linear dependences on the refractive index of the mixture solvent (Figure 5b). For the same reason as mentioned above for the plasmon linewidths, we also obtained the plasmon shifts in energy and plotted them as functions of the refractive index (Figure 5c). The plasmon shifts in energy also show approximately linear dependences on the refractive index. The RIS values were obtained by linearly fitting the plasmon shifts of the nanostructure samples. The FOM values were calculated

by use of the plasmon peak widths of the nanostructure samples dispersed in water. The results are plotted as functions of the added AgNO_3 volume in Figure 5d–g. In wavelength, upon Ag deposition, the RIS is increased (Figure 5d), mainly because at similar plasmon wavelengths, Ag nanoparticles possess higher RISs than Au nanoparticles.^[9] With increasing Ag deposition, the RIS first decreases and then increases. This trend is coincident with the change of the longitudinal plasmon wavelength (Figure 3b). It is mainly because for similarly shaped metal nanoparticles, longer plasmon wavelengths give rise to higher RISs.^[42] For the plot of the FOM values determined in the wavelength unit, Ag deposition causes an increase in the FOM (Figure 5e). As more Ag is deposited, the FOM decreases. There exists a certain amount of AgNO_3 (20 μL) that gives the largest FOM value. The decrease of the FOM after the maximal value is caused first by the reduction of the RIS and then by the increase of the plasmon linewidth. In energy, the RIS exhibits a large increase upon Ag deposition and then steady increases as more Ag is deposited (Figure 5f). This monotonous increase behavior in the RIS values expressed in energy is distinct from the trend observed with the RIS values expressed in wavelength. In contrast, the FOM values determined in both the wavelength and energy units display almost identical variation trends, in spite of discrepancies in their absolute values (Figure 5e,g). The FOM values determined in the wavelength unit for the Au NBP@Ag nanostructure samples are in the range of 5.2–6.7 RIU^{-1} , with the 20 μL sample possessing the largest value. The FOM values determined in the wavelength unit in our work are among the highest that have been reported for colloidal plasmonic metal nanoparticles in solutions at the ensemble level.^[44] Such high FOM values suggest that our Au NBP@Ag nanostructures have great potential in the development of high-performance plasmonic sensors.

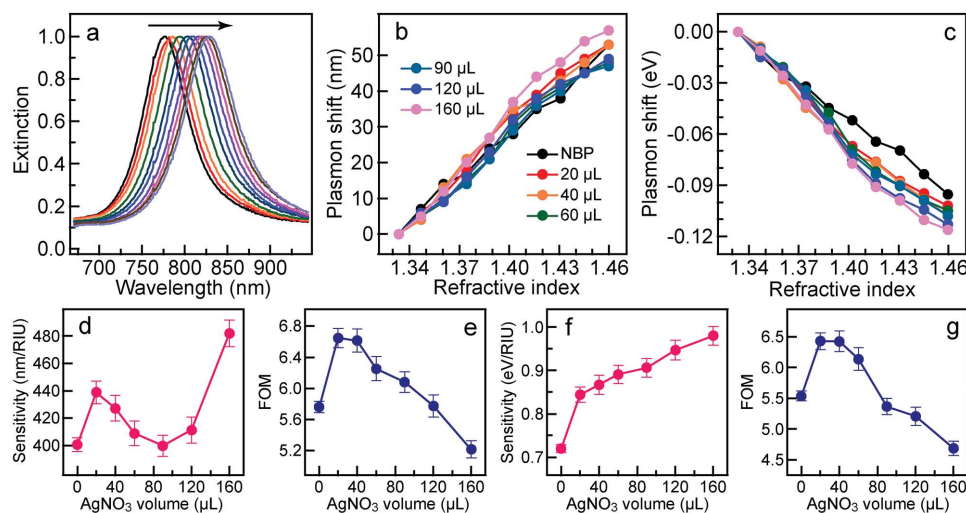


Figure 5. Refractive index sensing characteristics of the Au NBP@Ag nanostructures. a) Extinction spectra of the 20 μL sample dispersed in the water–glycerol liquid mixtures of varying compositions. Each spectrum has been normalized against its extinction peak intensity. The arrow indicates the direction of the increase in the refractive index of the solvent mixture as well as that of the shift of the longitudinal plasmon peak. b,c) Dependences of the longitudinal plasmon shifts in wavelength and energy on the refractive index of the liquid mixture, respectively. d) Plot of the RISs in wavelength against the AgNO_3 volume. e) FOM values calculated in the wavelength unit. f) RISs in energy. g) FOM values calculated in the energy unit. The labels in panel (b) also apply for panels (a) and (c). The error bar height for each point represents one standard deviation.

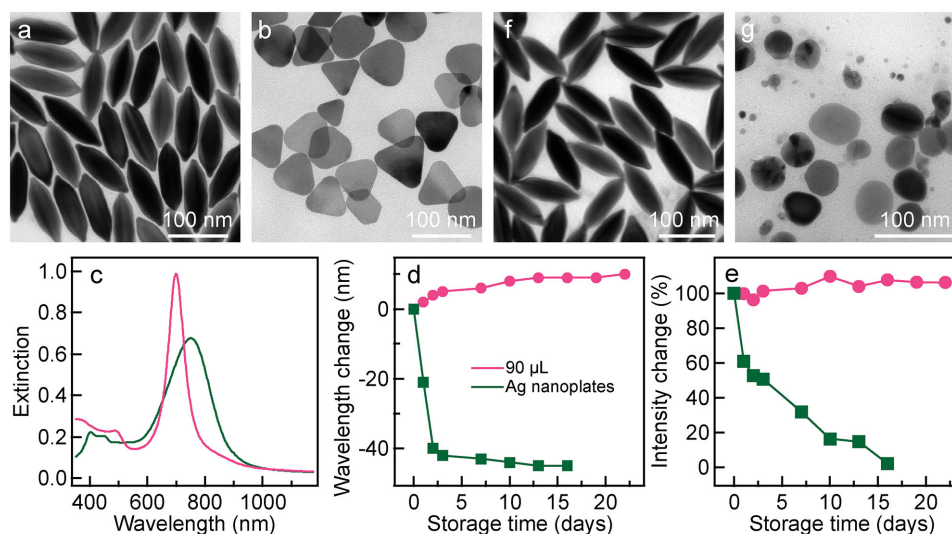


Figure 6. Stability tests. a,b) TEM images of the 90 μ L Au NBP@Ag nanostructures and Ag nanoplates, respectively. c) Extinction spectra of the Au NBP@Ag nanostructures and Ag nanoplates dispersed in aqueous solutions before aging. d) Plots of the extinction peak wavelengths as functions of the storage time. The peak wavelengths have been subtracted with those before aging. e) Plots of the extinction peak intensities as functions of the storage time. The extinction peak intensities have been normalized against the corresponding values before aging. The labels in panel (d) also apply for panel (e). f,g) TEM images of the Au NBP@Ag nanostructures and Ag nanoplates after they were kept at room temperature for 22 and 16 d, respectively.

2.4. Stability of the Au NBP@Ag Nanostructures

The structural and optical stabilities of metal nanoparticles are crucial for many practical applications. The nanoparticle shape has been well known to play an important role in determining the plasmonic properties of metal nanoparticles and therefore affect practical plasmonic applications. The thermodynamic instability poses a grand challenge for the preservation of Ag nanostructures in particular shapes in aqueous solutions.^[45] Ag nanoplates, which possess much narrower plasmon linewidths than many other types of Ag nanostructures, are unstable thermodynamically. They tend to transform spontaneously into other shapes with lower surface energies during storage.^[19,20] As a new type of Ag nanostructures with narrower plasmon linewidths than Ag nanoplates, our Au NBP@Ag nanostructures were examined and compared with Ag nanoplates in terms of their stability. The 90 μ L nanostructure sample was taken as an example. Triangular Ag nanoplates were prepared by a modified seed-mediated method.^[46] Their sizes were comparable to those prepared by laser excitation, which have the highest quality among all Ag nanoplate samples demonstrated so far.^[18] Both the Au NBP@Ag nanostructure and Ag nanoplate samples were washed once to remove excess surfactant molecules and then aged at room temperature for different periods of time. The Au NBP@Ag nanostructures have the rice shape while most of the Ag nanoplates are triangular with rounded corners (Figure 6a,b). Their major plasmon peak wavelengths are located at 700 and 750 nm, respectively (Figure 6c).

The extinction spectra of the two samples during the aging process in aqueous solutions were monitored and shown in Figure S7 in the Supporting Information. The extinction peak of the Ag nanoplates was too weak to be detected after 16 d of aging. In contrast, the extinction peak intensity of the Au NBP@Ag nanostructures remained unchanged even

after 22 d. For better comparison, the peak wavelength and intensity of the two samples were extracted from their time-dependent extinction spectra and plotted as functions of the aging time (Figure 6d,e). The plasmon peak of the Au NBP@Ag nanostructures shows a slight red shift of 10 nm within 22 d, while that of the Ag nanoplates blueshifts rapidly by approximately 40 nm in the first three days and then exhibits a slight blue shift of approximately 5 nm within next 13 d. No clear change of the extinction peak intensity is seen for the Au NBP@Ag nanostructures, while the extinction peak intensity of the Ag nanoplates undergoes a decline and approaches to zero after 16 d. We examined the Au NBP@Ag and Ag nanoplate samples under TEM after 22 and 16 d of storage, respectively. The shape and size of the Au NBP@Ag nanostructures were found to remain almost unchanged (Figure 6f). The slight red shift on the extinction peak of the Au NBP@Ag nanostructures might be caused by the detachment of a tiny amount of Ag from the nanostructures. There are two possible reasons for the high stability of the Au NBP@Ag nanostructures. One is the large electronegativity of Au, which can reduce the electron density on the Ag part and therefore make the Ag part difficult to be attached by O_2 dissolved in aqueous solutions.^[47–49] The other is the charge redistribution from the 4s orbitals to the 3d orbitals for Ag atoms upon alloying with Au.^[50] The reduced electron density in the 4s subshell increases the resistance of Ag to oxidation. In contrast, rounded and shrunk Ag nanoplates as well as much smaller spherical Ag nanoparticles are existent in the Ag nanoplate sample after storage (Figure 6g). The initial rapid blue shift in the extinction peak of the Ag nanoplates is believed to be caused by the rounding process. The slight blue shift, accompanied with the intensity reduction, at the later stage is believed to result from the fragmentation of the rounded Ag nanoplates into small spherical Ag nanoparticles. The results from the stability tests unambiguously show that our Au NBP@Ag nanostructures are highly

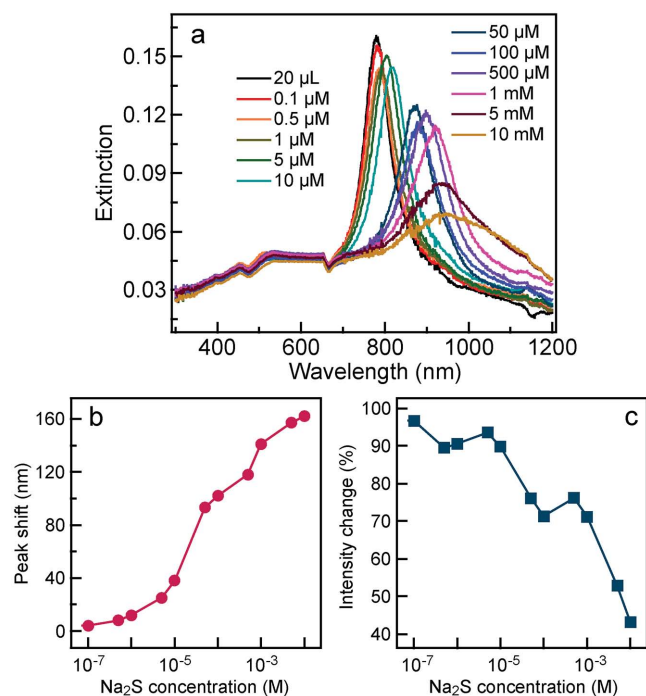


Figure 7. Sensing of sulfide ions with the 20 μL Au NBP@Ag nanostructures at the ensemble level. a) Extinction spectra of the nanostructures recorded after the addition of Na_2S at different concentrations. b) Dependence of the extinction peak shift on the Na_2S concentration. The peak shift was calculated relative to the plasmon wavelength of the nanostructures before Na_2S addition. c) Dependence of the intensity change on the Na_2S concentration. The peak intensity of each spectrum has been normalized against that of the spectrum recorded before Na_2S addition.

stable when kept in aqueous solutions, which is advantageous for their plasmon-based applications.

2.5. Sulfide Detection Using the Au NBP@Ag Nanostructures

H_2S has traditionally been considered as a corrosive and toxic gas with the unpleasant smell of rotten eggs. It is mainly produced by the decomposition of organics or as by-products of chemical processes. In addition, recent studies have shown H_2S as another gaseous transmitter besides NO and CO for its vital roles in fundamental signaling processes involved in human health and diseases.^[51,52] Therefore, the design of new and improved methods for detection of sulfide ions is of biological and medical interests.^[53] In the presence of O_2 , sulfide ions have been known to selectively and quickly react with Ag atoms to generate Ag_2S at room temperature.^[54,55] Therefore, our Au NBP@Ag nanostructures can be used for sulfide detection. The Ag part reacts with sulfide ions, causing structure and composition changes and in turn plasmonic changes. The changes can then be revealed spectrally.

Figure 7a shows the extinction spectra of the 20 μL Au NBP@Ag nanostructure sample exposed to Na_2S at different concentrations. The sulfide concentration employed in our experiments ranged from 0.1×10^{-6} to 10×10^{-3} M, covering a difference of five orders of magnitude. At 30 min after the addition of Na_2S , the longitudinal plasmon peak, which is located at

780 nm originally, shifts to longer wavelengths with decreasing intensities. The peak wavelengths and intensities were extracted and plotted against the concentration of Na_2S in Figure 7b,c, respectively. The plasmon peak redshifts with increasing Na_2S concentrations. A detection limit of 0.1×10^{-6} M is achieved. This detection limit is close to that obtained in a recent study with (Au nanorod core)@(Ag shell) nanostructures at the ensemble level.^[17] The extinction peak is seen to gradually decrease in intensity and become broader as the Na_2S concentration is increased. The spectral dependence on the Na_2S concentration can be attributed to two factors. One is the structural change caused by sulfidation, because as discussed above, the plasmon wavelength of the Au NBP@Ag nanostructures varies largely with the amount of deposited Ag atoms. The other is the change in the surrounding dielectric environment of the Au NBP@Ag nanostructures if they are covered with a layer of Ag_2S . Although the amount of Ag_2S is small, the Ag_2S layer is right on the surfaces of the nanostructures, where the local electric field enhancement is the largest. The peak broadening and intensity reduction are ascribed mainly to the plasmon damping induced by Ag_2S , because Ag_2S is a semiconductor with a band gap of ≈ 1.0 eV. The small band gap causes Ag_2S to absorb light strongly in the visible and near-infrared regions. Therefore, Ag_2S has a large imaginary part of the dielectric function in these spectral regions (Supporting Information, Figure S8).^[56] The plasmon damping gets more severe when more Ag_2S is formed on the metal nanostructures. In addition, the sulfidation is expected to differ among the different nanoparticles. This inhomogeneous sulfidation also causes plasmon peak broadening.

The reason for the similar detection limits between our work and the previous one^[17] at the ensemble level is that the Au@Ag nanostructures themselves are changed upon sulfidation. When plasmonic metal nanostructures are utilized for molecular sensing, metal nanostructures remain unchanged upon molecular adsorption. The detection limit of molecules is determined by the index sensitivity of metal nanostructures. In the detection of sulfide ions with the Au@Ag nanostructures, the Ag component is either partially or completely transformed from Ag metal into Ag_2S semiconductor, depending on the sulfide concentration. In our work, Ag atoms are mainly deposited on the side surface of the Au NBPs. In contrast, in the previous work,^[17] Ag atoms are deposited at both the side and end surfaces of the Au nanorods. Upon sulfidation, for our Au NBP@Ag nanostructures, each particle is only partially covered with Ag_2S . However, for the (Au nanorod core)@(Ag shell) nanostructures, each particle is encapsulated completely with a layer of Ag_2S . Therefore, even though the index sensitivities of our Au NBP@Ag nanostructures are believed to be higher than those of the (Au nanorod core)@(Ag shell) nanostructures, the detection limits of S^{2-} are similar.

The sulfide sensing experiments were also performed with the other Au NBP@Ag nanostructure samples. The results are given in Figures S9–S13 in the Supporting Information. With the nanostructures containing more Ag, the plasmon shifts tend to show abrupt increases at higher concentrations of Na_2S (Figures S10–S13, Supporting Information). In addition, the plasmon peak is almost completely damped at higher concentrations of Na_2S . The occurrence of the complete

plasmon damping is because a thicker layer of Ag₂S will be formed for the Au NBP@Ag nanostructures with more Ag at high concentrations of Na₂S. To fully understand the spectral variation behaviors of the different nanostructures at different concentrations of Na₂S will require more elaborate and systematic studies. Nevertheless, our results show that the nanostructures containing less Ag will be more suitable for sulfide detection.

3. Conclusions

We have successfully prepared Au NBP-supported Ag nanostructures with narrow plasmon linewidths and improved chemical stability. As the supplied amount of the Ag precursor is increased, the nanostructures undergo a shape evolution from NBP through nanorice to nanorod upon Ag overgrowth, suggesting that Ag atoms are preferentially deposited on the side surfaces of the Au NBPs. The accompanying spectral evolutions of the Au NBP@Ag nanostructures acquired at both the ensemble and single-particle levels indicate that with a relatively small amount of Ag deposited, the nanostructures are nearly monodisperse without inhomogeneous line broadening. The shape and size inhomogeneities start to take effect when a higher amount of Ag is overgrown on the Au NBPs. Systematic determination of the RIS and FOM values in both the wavelength and energy units shows that the RIS in energy increases as more Ag is overgrown on the Au NBPs. There exists an appropriate amount of deposited Ag atoms for the nanostructures to exhibit a maximal FOM, whose value determined in the wavelength unit is among the highest that have been reported for colloidal plasmonic metal nanoparticles in solutions at the ensemble level. Moreover, our nanostructures are found to possess a higher chemical stability than Ag nanoplates at a close ensemble plasmon wavelength. The use of the Au NBP@Ag nanostructures in the detection of sulfide ions is finally demonstrated, with a detection limit of 0.1×10^{-6} M. Taken together, our results show that the Au NBP@Ag nanostructures can be a promising candidate in the development of highly sensitive plasmonic sensors as well as in various plasmon-enhanced spectroscopies.

4. Experimental Section

Chemicals: HAuCl₄·3H₂O (99%), NaBH₄ (98%), trisodium citrate (99%), ascorbic acid (99%), AgNO₃ (99%), and poly(sodium 4-styrenesulfonate) (PSS, MW: ≈1 000 000) were purchased from Sigma-Aldrich. CTAB (98%) was obtained from Alfa Aesar. NH₃·H₂O solution (25 wt%) and HCl solution (5 M) were ordered from E. Merck and Scharlab, respectively. H₂O₂ solution (30 wt%) and CTAC (97%) were purchased from Aladdin Reagent. Deionized water with a resistivity of 18.2 MΩ cm obtained from a Direct-Q 5 UV water purification system was used in all experiments.

Preparation of the Au NBPs: The Au NBP sample was prepared using the seed-mediated growth method, as described in previous works.^[21,32] Briefly, a freshly prepared, ice-cold NaBH₄ solution (0.01 M, 0.15 mL) was added under vigorous stirring into an aqueous solution that was pre-made by mixing together HAuCl₄ (0.01 M, 0.125 mL), trisodium citrate (0.01 M, 0.25 mL), and water (9.625 mL). The resultant seed solution was kept at room temperature for 2 h before use. The seed

solution (0.2 mL) was injected into the growth solution that was made in advance by mixing together CTAB solution (0.1 M, 40 mL), HAuCl₄ (0.01 M, 2 mL), AgNO₃ (0.01 M, 0.4 mL), HCl (1 M, 0.8 mL), and ascorbic acid (0.1 M, 0.32 mL), followed by gentle inversion mixing for 10 s. The reaction solution was left undisturbed overnight at room temperature. The longitudinal plasmon wavelength of the obtained Au NBP sample was ≈805 nm. The purification of the as-prepared Au NBPs was conducted by using a depletion-induced separation method, as reported in a previous work.^[22] The number percentage of Au NBPs in the purified product was found from the TEM images to be 99%. The particle concentration of the purified Au NBP sample used in our experiments was adjusted to be 4.8×10^{10} particles mL⁻¹ on the basis of the Au mass concentration measured by ICP-AES and the average nanocrystal size determined from the TEM images.

Preparation of the Au NBP@Ag Nanostructures: The purified Au NBPs (5 mL) were centrifuged at 7000 rpm for 10 min. The precipitate was redispersed in a CTAC solution (0.08 M, 20 mL), followed by subsequent addition and mixing of AgNO₃ (0.01 M) and ascorbic acid (0.1 M). The volumes of the AgNO₃ solution were 20, 40, 60, 90, 120 and 160 μL for the samples shown in Figure 1, respectively. The volume of the ascorbic acid solution was a half of that of the AgNO₃ solution for each overgrowth. The mixture solution was placed in an air-bath shaker (60 °C, 120 revolutions per minute) and kept for 4.5 h, during which Ag was overgrown on the Au NBPs to form Au NBP@Ag nanostructures. The resultant samples were centrifuged at 5000–6500 rpm for 15 min. The precipitate was redispersed in water (10 mL) for further use.

Preparation of the Ag Nanoplates: Triangular Ag nanoplates were prepared by a modified seed-mediated growth method.^[46] In a typical preparation, Ag seeds were produced by combining trisodium citrate (2.5×10^{-3} M, 5 mL), PSS (1 g L⁻¹, 0.125 mL), and a freshly prepared, ice-cold NaBH₄ (0.01 M, 0.3 mL), followed by the addition of AgNO₃ (0.5×10^{-3} M, 5 mL) at a rate of 2 mL min⁻¹ under continuous stirring. The Ag nanoplates were produced by combining water (5 mL), ascorbic acid (0.01 M, 75 μL), and the seed solution (40 μL), followed by the addition of AgNO₃ (0.5×10^{-3} M, 3 mL) at a rate of 1 mL min⁻¹. Trisodium citrate (0.01 M, 1 mL) was subsequently added to stabilize the particles. The resultant sample was centrifuged once at 4000 rpm for 10 min and then redispersed in water (5 mL) for further use.

Stability Tests: The Au NBP@Ag nanostructures and Ag nanoplates were placed in 15 mL plastic centrifuge tubes and then aged at room temperature for varying periods of time. 1 mL of the solution was taken out from time to time for extinction measurements.

Refractive Index Sensitivity Measurements: To determine the RISs, the Au NBP@Ag nanostructures were centrifuged at 6000 rpm for 10 min and then redispersed into the water–glycerol mixture solvents of varying volume ratios. The volume percentage of glycerol in the liquid mixture was varied from 0% to 90% at a step of 10%. The extinction spectra of the Au NBP@Ag nanostructure samples dispersed in the mixture solvents were measured. The extinction peak shifts relative to the plasmon wavelengths of the nanostructure samples dispersed in water were calculated and plotted as functions of the refractive index. The RISs were obtained by linear fitting. The FOM values were obtained by dividing the RISs with the FWHM values determined from the extinction spectra of the aqueous dispersions of the Au NBP@Ag nanostructure samples.

Sulfide Sensing: For the detection of sulfide ions, the Au NBP@Ag nanostructure solution (10 mL) was placed in a 15 mL plastic centrifuge tube. An aqueous Na₂S solution (0.1 mL) at different concentrations was then added dropwise to the nanostructure solution within 5 s. The final concentration of Na₂S in the mixture solution was adjusted from 0.1×10^{-6} to 10×10^{-3} M. After the mixture solution was kept under continuous shaking for 30 min, the extinction spectra were recorded. Our extinction measurements showed that the sulfidation reaction for the 90 μL Au NBP@Ag nanostructure sample at different Na₂S concentrations took several minutes to reach a plateau. We therefore chose 30 min to make sure that the sulfidation reaction reached a steady state before the extinction measurement for all of the Au NBP@Ag nanostructure samples at different Na₂S concentrations.

Instrumentation: Extinction spectra were measured on a Hitachi U-3501 ultraviolet/visible/near-infrared spectrophotometer with plastic cuvettes of 0.5 cm optical path length. SEM imaging was performed on an FEI Quanta 400 FEG microscope operated at 20 kV. TEM imaging was carried out on an FEI Tecnai Spirit microscope operated at 120 kV. HAADF-STEM imaging and elemental mapping were carried out on an FEI Tecnai F20 microscope operated at 200 kV and equipped with an Oxford energy-dispersive X-ray analysis system. ICP-AES measurements were performed on a PerkinElmer Optima 4300DV system. Single-particle dark-field scattering images and spectra were recorded on an upright optical microscope (Olympus, BX60) that was integrated with a quartz-tungsten-halogen lamp (100 W), a monochromator (Acton, SpectraPro 2360i), and a charge-coupled device camera (Princeton Instruments, Pixa 400). During the measurements, the camera was thermoelectrically cooled to -70°C . A dark-field objective (100 \times , numerical aperture 0.9) was employed for both exciting the individual Au NBP@Ag nanostructures with the unpolarized white light and collecting the scattered light. The scattering spectrum from an individual nanoparticle was corrected by first subtracting the background spectrum taken from the adjacent region without any nanoparticles and then dividing it with the precalibrated response curve of the entire optical system. The exposure time was set at 30 s.

FDTD Simulations: The FDTD simulations of the Au NBP@Ag nanostructures were performed using FDTD Solutions 8.7, which was developed by Lumerical Solutions, Inc. During the simulations, an electromagnetic plane wave in the spectral range from 300 to 1200 nm was launched into a box containing a target nanostructure. A mesh size of 0.5 nm was employed in calculating the extinction spectra of the Au NBP@Ag nanostructures. The refractive index of the surrounding medium was set to be 1.33, the refractive index of water. The dielectric function of Au was obtained by fitting the measured data of Johnson and Christy, and that of Ag was fitted from Palik's data. For the purpose of simplification, the Au NBP was modeled as being composed of two circular cones with spherically rounded tips, using the average diameters and lengths determined from the TEM images. The two cones were back-to-back stacked together. Such a simplified geometrical model has been shown to be able to simulate the plasmonic properties of various sized Au NBPs in reasonably good agreement with experiments.^[22,57] The diameter and length of the Au NBP were set at 39 and 122 nm, respectively. The tip angle and radius were adjusted to be 30° and 6 nm, respectively, to match the simulated longitudinal dipolar plasmon wavelength with the experimental values. To model the Au NBP@Ag nanostructures, Ag atoms were placed at the side surfaces of the Au NBP by employing a parabola cone together with an end-rounded cylinder and adjusting their geometrical parameters. Except the 20 μL Au NBP@Ag nanostructure sample, the thickness of the Ag layer at the middle of the nanostructures was set at 1.5 nm, according to the TEM measurements. All of the considered models are shown in Figure 3f. Because we were interested in the variation behaviors of the longitudinal plasmon positions and linewidths, the excitation light direction was set perpendicular to the length axis, with the electric field aligned along the length axis.

Supporting Information

Supporting Information is available from the Wiley Online Library or from the author.

Acknowledgements

This work was supported by the Program for Professor of Special Appointment (Eastern Scholar) at Shanghai Institutions of Higher Learning and a Hong Kong RGC CRF grant (Ref. No.: CUHK4/CRF/12G).

Received: August 30, 2015

Revised: October 9, 2015

Published online: November 23, 2015

- [1] V. Giannini, A. I. Fernández-Domínguez, S. C. Heck, S. A. Maier, *Chem. Rev.* **2011**, *111*, 3888.
- [2] K. M. Mayer, J. H. Hafner, *Chem. Rev.* **2011**, *111*, 3828.
- [3] K. Saha, S. S. Agasti, C. Kim, X. N. Li, V. M. Rotello, *Chem. Rev.* **2012**, *112*, 2739.
- [4] R. B. Jiang, B. X. Li, C. H. Fang, J. F. Wang, *Adv. Mater.* **2014**, *26*, 5274.
- [5] X. H. Huang, S. Neretina, M. A. El-Sayed, *Adv. Mater.* **2009**, *21*, 4880.
- [6] H. A. Atwater, A. Polman, *Nat. Mater.* **2010**, *9*, 205.
- [7] S. Lal, N. K. Grady, J. Kundu, C. S. Levin, J. B. Lassiter, N. J. Halas, *Chem. Soc. Rev.* **2008**, *37*, 898.
- [8] A. Jakab, C. Rosman, Y. Khalavka, J. Becker, A. Trügler, U. Hohenester, C. Sönnichsen, *ACS Nano* **2011**, *5*, 6880.
- [9] Y. H. Lee, H. J. Chen, Q.-H. Xu, J. F. Wang, *J. Phys. Chem. C* **2011**, *115*, 7997.
- [10] K.-S. Lee, M. A. El-Sayed, *J. Phys. Chem. B* **2006**, *110*, 19220.
- [11] K. Sugawa, H. Tahara, A. Yamashita, J. Otsuki, T. Sagara, T. Harumoto, S. Yanagida, *ACS Nano* **2015**, *9*, 1895.
- [12] S. Gómez-Graña, J. Pérez-Juste, R. A. Alvarez-Puebla, A. Guerrero-Martínez, L. M. Liz-Marzán, *Adv. Opt. Mater.* **2013**, *1*, 477.
- [13] P. Bharadwaj, L. Novotny, *Opt. Express* **2007**, *15*, 14266.
- [14] F. M. Wang, N. A. Melosh, *Nano Lett.* **2011**, *11*, 5426.
- [15] D. E. Charles, D. Aherne, M. Gara, D. M. Ledwith, Y. K. Gun'ko, J. M. Kelly, W. J. Blau, M. E. Brennan-Fournet, *ACS Nano* **2010**, *4*, 55.
- [16] C. Zhang, A.-X. Yin, R. B. Jiang, J. Rong, L. Dong, T. Zhao, L.-D. Sun, J. F. Wang, X. Chen, C.-H. Yan, *ACS Nano* **2013**, *7*, 4561.
- [17] B. Xiong, R. Zhou, J. R. Hao, Y. H. Jia, Y. He, E. S. Yeung, *Nat. Commun.* **2013**, *4*, 1708.
- [18] R. C. Jin, Y. C. Cao, E. C. Hao, G. S. Métraux, G. C. Schatz, C. A. Mirkin, *Nature* **2003**, *425*, 487.
- [19] Q. Zhang, J. P. Ge, T. Pham, J. Goebel, Y. X. Hu, Z. D. Lu, Y. D. Yin, *Angew. Chem., Int. Ed.* **2009**, *48*, 3516.
- [20] J. Zeng, S. Roberts, Y. N. Xia, *Chem. - Eur. J.* **2010**, *16*, 12559.
- [21] X. S. Kou, W. H. Ni, C.-K. Tsung, K. Chan, H.-Q. Lin, G. D. Stucky, J. F. Wang, *Small* **2007**, *3*, 2103.
- [22] Q. Li, X. L. Zhuo, S. Li, Q. F. Ruan, Q.-H. Xu, J. F. Wang, *Adv. Opt. Mater.* **2015**, *3*, 801.
- [23] X. S. Kou, S. Z. Zhang, C.-K. Tsung, M. H. Yeung, Q. H. Shi, G. D. Stucky, L. D. Sun, J. F. Wang, C. H. Yan, *J. Phys. Chem. B* **2006**, *110*, 16377.
- [24] J.-H. Lee, K. J. Gibson, G. Chen, Y. Weizmann, *Nat. Commun.* **2015**, *6*, 7571.
- [25] M.-F. Tsai, S.-H. G. Chang, F.-Y. Cheng, V. Shanmugam, Y.-S. Cheng, C.-H. Su, C.-S. Yeh, *ACS Nano* **2013**, *7*, 5330.
- [26] H. J. Chen, L. Shao, Q. Li, J. F. Wang, *Chem. Soc. Rev.* **2013**, *42*, 2679.
- [27] R. B. Jiang, H. J. Chen, L. Shao, Q. Li, J. F. Wang, *Adv. Mater.* **2012**, *24*, OP200.
- [28] A. F. Smith, R. G. Weiner, M. M. Bower, B. Dragnea, S. E. Skrabalak, *J. Phys. Chem. C* **2015**, *119*, 22114.
- [29] T. Ming, X. S. Kou, H. J. Chen, T. Wang, H.-L. Tam, K.-W. Cheah, J.-Y. Chen, J. F. Wang, *Angew. Chem., Int. Ed.* **2008**, *47*, 9685.
- [30] T. Wang, J. Q. Zhuang, J. Lynch, O. Chen, Z. L. Wang, X. R. Wang, D. LaMontagne, H. M. Wu, Z. W. Wang, Y. C. Cao, *Science* **2012**, *338*, 358.
- [31] Y. H. Lee, W. X. Shi, H. K. Lee, R. B. Jiang, I. Y. Phang, Y. Cui, L. Isa, Y. J. Yang, J. F. Wang, S. Z. Li, X. Y. Ling, *Nat. Commun.* **2015**, *6*, 6990.
- [32] M. Z. Liu, P. Guyot-Sionnest, *J. Phys. Chem. B* **2005**, *109*, 22192.
- [33] Q. Li, R. B. Jiang, T. Ming, C. H. Fang, J. F. Wang, *Nanoscale* **2012**, *4*, 7070.
- [34] T. K. Sau, C. J. Murphy, *Langmuir* **2004**, *20*, 6414.

- [35] W. H. Ni, K. S. Kou, Z. Yang, J. F. Wang, *ACS Nano* **2008**, *2*, 677.
- [36] X. L. Zhuo, Z. Z. Zhu, Q. Li, Z. Yang, J. F. Wang, *ACS Nano* **2015**, *9*, 7523.
- [37] C. Sönnichsen, T. Franzl, T. Wilk, G. von Plessen, J. Feldmann, O. Wilson, P. Mulvaney, *Phys. Rev. Lett.* **2002**, *88*, 077042.
- [38] A. Hoggard, L.-Y. Wang, L. L. Ma, Y. Fang, G. You, J. Olson, Z. Liu, W.-S. Chang, P. M. Ajayan, S. Link, *ACS Nano* **2013**, *7*, 11209.
- [39] P. Zijlstra, P. M. R. Paulo, K. Yu, Q.-H. Xu, M. Orrit, *Angew. Chem., Int. Ed.* **2012**, *51*, 8352.
- [40] L. Shao, C. H. Fang, H. J. Chen, Y. C. Man, J. F. Wang, H.-Q. Lin, *Nano Lett.* **2012**, *12*, 1424.
- [41] L. J. Sherry, S.-H. Chang, G. C. Schatz, R. P. Van Duyne, *Nano Lett.* **2005**, *5*, 2034.
- [42] H. J. Chen, X. S. Kou, Z. Yang, W. H. Ni, J. F. Wang, *Langmuir* **2008**, *24*, 5233.
- [43] H. J. Chen, L. Shao, K. C. Woo, T. Ming, H.-Q. Lin, J. F. Wang, *J. Phys. Chem. C* **2009**, *113*, 17691.
- [44] Y. Shen, J. H. Zhou, T. R. Liu, Y. T. Tao, R. B. Jiang, M. X. Liu, G. H. Xiao, J. H. Zhu, Z.-K. Zhou, X. H. Wang, C. J. Jin, J. F. Wang, *Nat. Commun.* **2013**, *4*, 2381.
- [45] X. C. Jiang, Q. H. Zeng, A. B. Yu, *Langmuir* **2007**, *23*, 2218.
- [46] D. Aherne, D. M. Ledwith, M. Gara, J. M. Kelly, *Adv. Funct. Mater.* **2008**, *18*, 2005.
- [47] M. Tsuji, D. Yamaguchi, M. Matsunaga, M. J. Alam, *Cryst. Growth Des.* **2010**, *10*, 5129.
- [48] M. Tsuji, S. Hikino, R. Tanabe, M. Matsunaga, Y. Sano, *CrystEngComm* **2010**, *12*, 3900.
- [49] C. B. Gao, Y. X. Hu, M. S. Wang, M. F. Chi, Y. D. Yin, *J. Am. Chem. Soc.* **2014**, *136*, 7474.
- [50] J. F. Huang, Y. H. Zhu, C. X. Liu, Y. F. Zhao, Z. H. Liu, M. N. Hedhili, A. Fratalocchi, Y. Han, *Small* **2015**, DOI: 10.1002/smll.201501220.
- [51] Y. Qian, J. Karpus, O. Kabil, S.-Y. Zhang, H.-L. Zhu, R. Banerjee, J. Zhao, C. He, *Nat. Commun.* **2011**, *2*, 495.
- [52] W. M. Xuan, C. Q. Sheng, Y. T. Cao, W. H. He, W. Wang, *Angew. Chem., Int. Ed.* **2012**, *51*, 2282.
- [53] S. Chen, Z.-J. Chen, W. Ren, H.-W. Ai, *J. Am. Chem. Soc.* **2012**, *134*, 9589.
- [54] B. Liu, Z. F. Ma, *Small* **2011**, *7*, 1587.
- [55] C. H. Fang, Y. H. Lee, L. Shao, R. B. Jiang, J. F. Wang, Q.-H. Xu, *ACS Nano* **2013**, *7*, 9354.
- [56] J. M. Bennett, J. L. Stanford, E. J. Ashley, *J. Opt. Soc. Am.* **1970**, *60*, 224.
- [57] A. Lombardi, M. Loumaigne, A. Crut, P. Maioli, N. Del Fatti, F. Vallée, *Langmuir* **2012**, *28*, 9027.